

A Mononuclear, Nonheme Fe^{II}–Piloty's Acid (PhSO₂NHOH) Adduct: An Intermediate in the Production of {FeNO}^{7/8} Complexes from Piloty's Acid

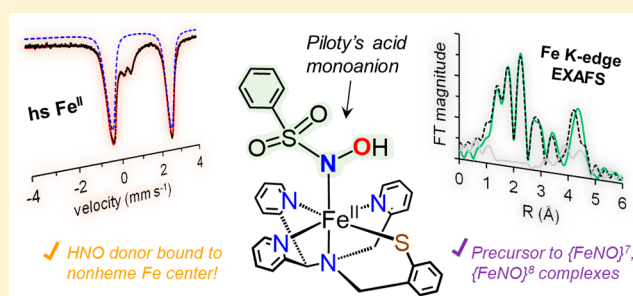
Alex M. Confer,[†] Avery C. Vilbert,[‡] Aniruddha Dey,[†] Kyle M. Lancaster,^{*,‡} and David P. Goldberg^{*,†}

[†]Department of Chemistry, The Johns Hopkins University, Baltimore, Maryland 21218, United States

[‡]Baker Laboratory, Department of Chemistry and Chemical Biology, Cornell University, Ithaca, New York 14853, United States

Supporting Information

ABSTRACT: Reaction of the mononuclear nonheme complex [Fe^{II}(CH₃CN)(N3PyS)]BF₄ (**1**) with an HNO donor, Piloty's acid (PhSO₂NHOH, P.A.), at low temperature affords a high-spin (*S* = 2) Fe^{II}–P.A. intermediate (**2**), characterized by ⁵⁷Fe Mössbauer and Fe K-edge X-ray absorption (XAS) spectroscopies, with interpretation of both supported by DFT calculations. The combined methods indicate that P.A. anion binds as the N-deprotonated tautomer (PhSO₂NOH[−]) to [Fe^{II}(N3PyS)]⁺, leading to **2**. Complex **2** is the first spectroscopically characterized example, to our knowledge, of P.A. anion bound to a redox-active metal center. Warming of **2** above −60 °C yields the stable {FeNO}⁷ complex [Fe(NO)(N3PyS)]BF₄ (**4**), as evidenced by ¹H NMR, ATR-IR, and Mössbauer spectroscopies. Isotope labeling experiments with ¹⁵N-labeled P.A. confirm that the nitrosyl ligand in **4** derives from P.A. In contrast, addition of a second equivalent of a strong base leads to S–N cleavage and production of an {FeNO}⁸ species, the deprotonated analog of an Fe–HNO complex. This work has implications for the targeted delivery of HNO/NO[−]/NO· to nonheme Fe centers in biological and synthetic applications, and suggests a new role for nonheme Fe^{II} complexes in the assisted degradation of HNO donor molecules.



INTRODUCTION

Nitroxyl (HNO/NO[−], also known as azanone or nitrosyl hydride) is an important biomolecule whose endogenous production and pharmacology have yet to be resolved.^{1–6} The HNO molecule is a positive cardiac inotrope used in the treatment of heart failure,⁷ and is also a potent inhibitor of aldehyde dehydrogenase,^{8–10} showing promise as a therapeutic for alcohol addiction. It is currently thought that HNO participates in signal transduction in biology by coordinating to the heme center in soluble guanylate cyclase.^{11,12} Metal-bound HNO species (Mⁿ⁺(HNO)) have been implicated as reactive intermediates in a number of catalytic cycles that process NO,^{13–15} but only a few examples of Mⁿ⁺(HNO) complexes with first row metals have been reported to date.^{16–26} HNO has also been used as a surrogate for O₂; for example, substitution of O₂ by HNO in reactions with the enzyme manganese quercetin 2,3-dioxygenase led to substrate nitroxygenation (i.e., HNO incorporation).^{27,28} Furthermore, there is considerable interest in the reduction/protonation of metal nitrosyl species (M(NO·)) to produce viable HNO-releasing agents, as well as to examine the feasibility of HNO production from metal centers and NO· *in vivo*.^{24,25,29–38}

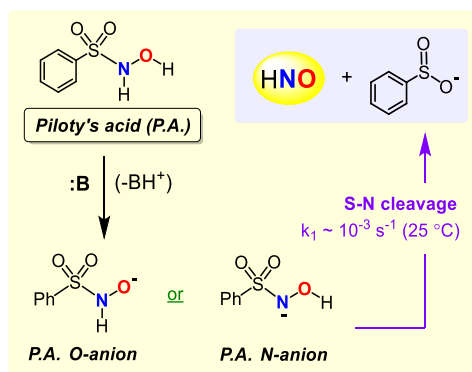
In contrast to NO·, which is relatively stable under anaerobic conditions, HNO has an intrinsically short lifetime due to

rapid ($8.0 \times 10^6 \text{ M}^{-1} \text{ s}^{-1}$)³⁹ dimerization to give hyponitrous acid, HON=NOH, which further decays to yield N₂O and H₂O ($8.0 \times 10^{-4} \text{ s}^{-1}$).⁴⁰ To deliver the short-lived HNO *in situ* for biochemical studies or medical applications, donor molecules that release HNO in response to external stimuli (e.g., pH, temperature, light) must be employed. Sulfohydroxamic acids (RSO₂NHOH, R = -alkyl, aryl) constitute one important class of HNO donors that release HNO mainly in response to pH,⁴¹ and in some cases, through photoactivation.^{42,43} Piloty's acid (*N*-hydroxybenzenesulfonamide; P.A.), first reported in 1896,⁴⁴ is the oldest member of this class, and releases HNO under basic conditions according to the mechanism shown in Scheme 1. However, donation of HNO by P.A. is slow ($k_{\text{max}} \sim 10^{-3}$ to 10^{-4} s^{-1} at 25 °C).⁴¹

Given that basic conditions are necessary to produce HNO, the P.A.[−] anion is presumed to be the immediate precursor to HNO release. There are two possible tautomers of monodeprotonated P.A.[−], either PhSO₂NOH[−] (N-deprotonated) or PhSO₂NHO[−] (O-deprotonated). Given the relatively slow rates of HNO release from P.A., we hypothesized that the P.A.[−] anion could be an important

Received: February 13, 2019

Scheme 1. Mechanism of HNO Release from Piloty's Acid



player in the reactivity with a cationic metal center. Precedent for this hypothesis comes from a high-resolution crystal structure of zinc carbonic anhydrase (human isoform II) inhibited by P.A.⁴⁵ This structure shows that P.A.⁻ anion binds to the active site by coordinating to the zinc(II) center through the sulfonamido N atom, i.e. the N-deprotonated tautomer. Alkali metal salts of P.A.⁻ anion (e.g., Li⁺, Na⁺) exist as the N-deprotonated tautomer in both the solid state and in dioxane solution,^{46,47} and there is computational evidence to suggest that this tautomer is energetically favored.⁴⁸ Other data suggest that it is the O-deprotonated tautomer that leads to HNO release.⁴⁹

The interactions of redox-active, biologically relevant metal ions such as Fe, Mn, or Co, with HNO donors such as P.A. have been examined previously, and in some cases, were shown to accelerate the decomposition of P.A. and related RSO₂NHOH compounds.^{48,50,51} However, there is still relatively little known about the mechanism of action between redox-active metal ions and RSO₂NHOH compounds. In particular, direct structural or spectroscopic evidence for metal–P.A. adducts is lacking. We have set out to examine nonheme iron complexes and their interaction with P.A. and other RSO₂NHOH donors in order to characterize the potential binding modes, mechanisms of action, and HNO-releasing properties of Fe/P.A. systems.

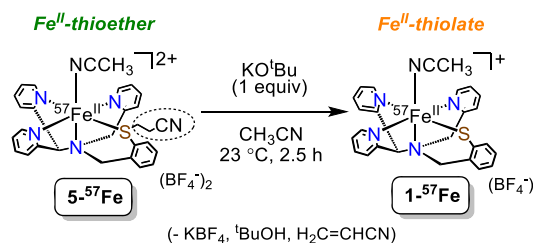
We previously described the reaction of an Fe^{II}–solvent complex, [Fe^{II}(CH₃CN)(N3PyS)]BF₄ (**1**) with P.A. in the presence of KO^tBu/18-crown-6 (1 equiv) at –40 °C. This reaction gave a new, thermally unstable species **2**, which was characterized by UV–vis spectroscopy ($\lambda_{\text{max}} = 418, 501 \text{ nm}$).²⁹ Reaction of **2** with a further equivalent of base at –40 °C afforded the {FeNO}⁸ complex [Fe(NO)(N3PyS)] (**3**) ($\lambda_{\text{max}} = 520, 720 \text{ nm}$), which was also obtained by one-electron reduction of an {FeNO}⁷ precursor, [Fe(NO)(N3PyS)]BF₄ (**4**), with decamethylcobaltocene (CoCp*₂). The {FeNO}⁸ complex **3** exhibited a rare *S* = 1 ground state,^{29,52} and was shown to produce N₂O in 54% yield upon standing in solution at 23 °C. We reasoned that complex **2**, the immediate precursor to the {FeNO}⁸ species, could be an Fe(HNO) or Fe–P.A. adduct, but no further spectroscopic characterization was obtained.

Herein we provide new characterization of **2** by ⁵⁷Fe Mössbauer and Fe K-edge X-ray absorption spectroscopies, which show that **2** is in fact a high-spin (*S* = 2) Fe^{II}–P.A. adduct. Density functional theory (DFT) calculations, including predicted Mössbauer parameters for N-bound Fe–P.A. adducts, support the spectroscopic results and suggest that

the P.A. ligand in **2** is coordinated through nitrogen. Using a combination of Mössbauer, paramagnetic ¹H NMR, and attenuated total reflectance infrared (ATR-IR) spectroscopies, we show that the thermal decay of **2** under strictly anaerobic conditions yields the {FeNO}⁷ complex **4**. In contrast, the {FeNO}⁸ complex **3** is produced from adding more base, consistent with **2** being a precursor to Fe(HNO).

RESULTS AND DISCUSSION

Synthesis and Solution State Properties of [⁵⁷Fe^{II}(CH₃CN)(N3PyS)]BF₄ (1**-⁵⁷Fe).** The Fe^{II}–thiolate starting material, [⁵⁷Fe^{II}(CH₃CN)(N3PyS)]BF₄ (**1**-⁵⁷Fe), was prepared from the isotopically enriched (⁵⁷Fe, 95%) Fe^{II}–thioether precursor, [⁵⁷Fe^{II}(CH₃CN)(N3PySEtCN)](BF₄)₂ (**5**-⁵⁷Fe) by using the method previously described for the normal abundance analogue (Scheme 2).²⁹ Treatment of

Scheme 2. Preparation of Isotopically Labeled [Fe^{II}(CH₃CN)(N3PyS)]BF₄ (**1**-⁵⁷Fe)

5-⁵⁷Fe with KO^tBu (1 equiv) in dry, deoxygenated CH₃CN at 23 °C produces an instantaneous color change from orange-red to wine-red, corresponding to removal of the base-labile 2-cyanoethyl protecting group from the sulfur donor. Pure **1**-⁵⁷Fe, a dark red-brown solid, is isolated in 65% crystalline yield after addition of excess diethyl ether to a concentrated CH₃CN/toluene (1:1 v/v) solution of the product.

The zero-field ⁵⁷Fe Mössbauer spectra of **5**-⁵⁷Fe and **1**-⁵⁷Fe, recorded at 80 K in frozen CH₃CN, are shown in Figure 1. Thioether-ligated **5**-⁵⁷Fe produces a sharp quadrupole doublet with $\delta = 0.44$ and $|\Delta E_{\text{Q}}| = 0.55 \text{ mm s}^{-1}$, consistent with a low-spin (*ls*, *S* = 0) Fe^{II} ground state. Thiolate-ligated **1**-⁵⁷Fe exhibits parameters ($\delta = 0.43$, $|\Delta E_{\text{Q}}| = 0.31 \text{ mm s}^{-1}$) that are also consistent with *ls* Fe^{II} and accord well with the data previously collected at 5.4 K for crystalline **1** ($\delta = 0.41$ and $|\Delta E_{\text{Q}}| = 0.26 \text{ mm s}^{-1}$).⁵³ This result provides strong evidence that **1** retains its mononuclear, six-coordinate, solid state structure upon dissolution in CH₃CN. The nearly identical isomer shifts observed for **5**-⁵⁷Fe and **1**-⁵⁷Fe (0.44 vs 0.43 mm s⁻¹) make good sense in light of the fact that these complexes possess very similar first coordination sphere metrics by single crystal X-ray diffraction. In the solid state, complexes **1** and **5** exhibit average Fe–N_{py} distances of 1.9594(13) Å and 1.9659(13) Å and Fe–S distances of 2.2848(4) and 2.3018(4) Å, respectively.^{53,54} Despite their similar overall coordination environments, **5**-⁵⁷Fe and **1**-⁵⁷Fe have different $|\Delta E_{\text{Q}}|$ values (0.55 vs 0.31 mm s⁻¹), which likely reflects the difference in thioether versus thiolate ligation.

Reactivity of **1 with Piloty's Acid.** It was shown previously that complex **1** reacted with Piloty's acid (P.A.) and KO^tBu/18-crown-6 in CH₃CN at –40 °C to give a new, thermally unstable intermediate **2**, which was characterized by UV–vis spectroscopy ($\lambda_{\text{max}} = 418, 501 \text{ nm}$).²⁹ This species is not observed when the reaction is run at 23 °C (*vide infra*).

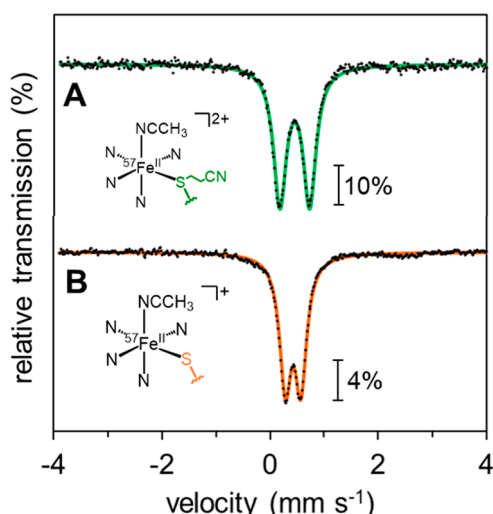
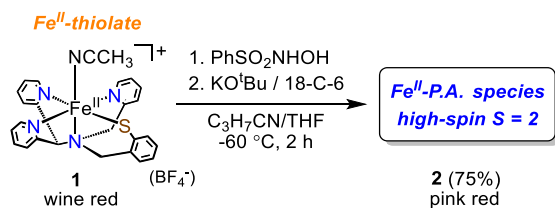


Figure 1. ^{57}Fe Mössbauer spectra (80 K in frozen CH_3CN) showing the conversion of $5\text{-}^{57}\text{Fe}$ to $1\text{-}^{57}\text{Fe}$ according to Scheme 2. Experimental data are plotted as black dots while best fits are overlaid as solid lines. (a) Spectrum of $5\text{-}^{57}\text{Fe}$ fit to a single doublet with $\delta = 0.44$, $|\Delta E_Q| = 0.55$, $\Gamma_{L=R} = 0.29$ mm s^{-1} . (b) Spectrum of $1\text{-}^{57}\text{Fe}$ fit to a single doublet with $\delta = 0.43$, $|\Delta E_Q| = 0.31$, $\Gamma_{L=R} = 0.25$ mm s^{-1} .

We hypothesized that this intermediate might be either an $\text{Fe}(\text{HNO})$ or $\text{Fe}(\text{P.A.})$ adduct, but no further spectroscopic characterization was obtained. With $1\text{-}^{57}\text{Fe}$ in hand, intermediate $2\text{-}^{57}\text{Fe}$ could be examined by Mössbauer spectroscopy. To increase the stability of $2\text{-}^{57}\text{Fe}$, we changed to a mixed solvent system of *n*-butyronitrile/THF, which allowed for lower temperatures to be employed and for the solubility of $\text{KO}^t\text{Bu}/18\text{-crown-6}$ to be maintained.

The generation of $2\text{-}^{57}\text{Fe}$ at ca. -60 °C in $\text{C}_3\text{H}_7\text{CN}/\text{THF}$ is outlined in Scheme 3. Anaerobic, dropwise addition of a THF

Scheme 3. Reaction of $[\text{Fe}^{\text{II}}(\text{CH}_3\text{CN})(\text{N3PyS})]\text{BF}_4$ and Piloty's Acid at -60 °C



solution of $\text{KO}^t\text{Bu}/18\text{-crown-6}$ (1 equiv) to a precooled mixture of $1\text{-}^{57}\text{Fe}$ (5 mM) and P.A. (1 equiv) in $\text{C}_3\text{H}_7\text{CN}$ produces a gradual color change from deep wine red to bright pink red over 2 h. This color change is due to loss of the intense charge-transfer bands for diamagnetic **1** ($\epsilon \sim 4000\text{--}5000$ $\text{M}^{-1}\text{cm}^{-1}$)⁵³ as intermediate **2** ($\epsilon \sim 1000$ $\text{M}^{-1}\text{cm}^{-1}$) is formed, as shown previously. An aliquot of the cold, deoxygenated reaction mixture can be quickly transferred to a Mössbauer sample holder using air-free techniques. Alternatively, the reaction mixture can be rapidly frozen by pouring into liquid N_2 , giving frozen pellets which then can be further pulverized to give a fine powder that is loaded into the Mössbauer sample holder.

A representative Mössbauer spectrum for the reaction mixture is shown in Figure 2. The major species, which accounts for 75% of the fitted area, has parameters consistent

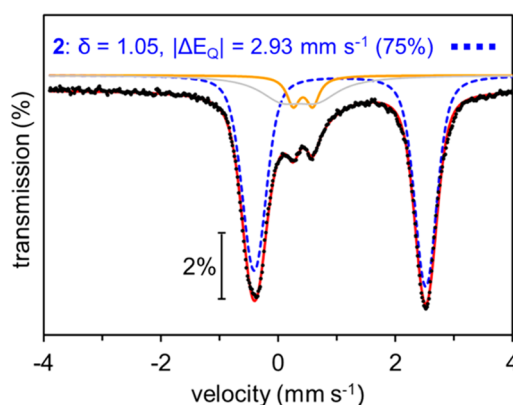
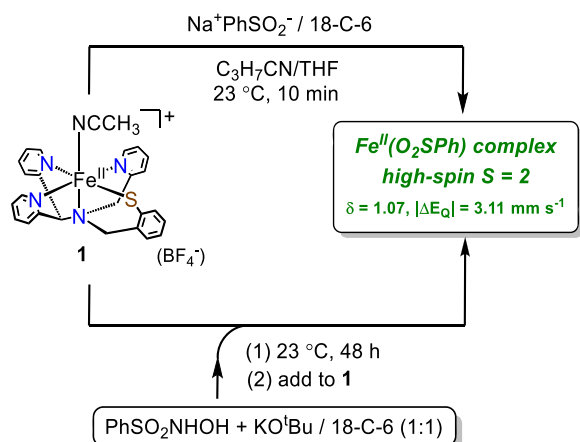


Figure 2. ^{57}Fe Mössbauer spectrum (80 K, $\text{C}_3\text{H}_7\text{CN}/\text{THF}$, 9:1 v/v) of $1\text{-}^{57}\text{Fe}$ + P.A. (1 equiv) + $\text{KO}^t\text{Bu}/18\text{-crown-6}$ (1 equiv) reacted at -60 °C for 2 h according to Scheme 3. Experimental data (black dots); best fit (red line); majority hs Fe^{II} species $2\text{-}^{57}\text{Fe}$ (dashed blue line, 75%; Voigt line shape); minor ls Fe^{II} species (solid orange line, 7%; Lorentzian line shape) corresponding to $1\text{-}^{57}\text{Fe}$; minor species (solid gray line, 18%) corresponding to an unidentified product.

with a hs Fe^{II} species ($\delta = 1.05$, $|\Delta E_Q| = 2.93$ mm s^{-1} ; dashed blue line). We assign this doublet to $2\text{-}^{57}\text{Fe}$. A minor component corresponds to starting $1\text{-}^{57}\text{Fe}$ ($\delta = 0.42$, $|\Delta E_Q| = 0.33$ mm s^{-1} ; solid orange line, 7% of fit). A third, broad component with $\delta = 0.36$ and $|\Delta E_Q| = 0.61$ mm s^{-1} (18%) is required to fit the remaining area and corresponds to an unidentified product. Longer reaction times (3–6 h), or lower temperature (-80 °C), did not significantly increase the spectroscopic yield of $2\text{-}^{57}\text{Fe}$.

Our group has shown that an analogous change from low-spin to high-spin Fe^{II} occurs when **1** is dissolved in methanol.^{53,55} This hs Fe^{II} species was assigned as $[\text{Fe}^{\text{II}}(\text{CH}_3\text{OH})(\text{N3PyS})]^+$ (**1-CH₃OH**). The 80 K Mössbauer spectrum for $1\text{-}^{57}\text{Fe}$ dissolved in methanol contains two quadrupole doublets, one arising from the acetonitrile-bound species (60%), and the other arising from the proposed methanol adduct ($\delta = 1.05$, $|\Delta E_Q| = 2.77$ mm s^{-1} ; 40%) (Figure S1). At room temperature, the CH_3CN in **1** is completely displaced by CH_3OH as evidenced by Evans method measurements,⁵³ and the Mössbauer data show that upon freezing the rebinding of CH_3CN is greatly favored. In contrast, the P.A.-derived ligand readily outcompetes either CH_3CN or the related $\text{C}_3\text{H}_7\text{CN}$ solvent for the Fe binding site. Notably, the isomer shifts for $1\text{-}^{57}\text{Fe}$ in CH_3OH and $2\text{-}^{57}\text{Fe}$ are identical, which indicates that their overall coordination environments are similar. The combined observations suggest that binding of the reactive P.A. species to Fe is favored over CH_3CN , and maintains the $[\text{Fe}^{\text{II}}(\text{N3PyS})]^+$ core structure.

As shown in Scheme 1, HNO release from Piloty's acid is accompanied by generation of benzenesulfinate anion (PhSO_2^-), a possible ligand for $[\text{Fe}^{\text{II}}(\text{N3PyS})]^+$. To test whether $2\text{-}^{57}\text{Fe}$ is an $\text{Fe}^{\text{II}}\text{-PhSO}_2^-$ adduct rather than a P.A. or HNO adduct, $1\text{-}^{57}\text{Fe}$ was reacted with $\text{Na}^+\text{PhSO}_2^-$ according to Scheme 4. This reaction yielded a new, thermally stable hs Fe^{II} species ($6\text{-}^{57}\text{Fe}$) with $\delta = 1.07$ and $|\Delta E_Q| = 3.11$ mm s^{-1} , which we assign to a coordinated $\text{Fe}^{\text{II}}(\text{O}_2\text{SPh})$ adduct. Importantly, these parameters are significantly different from those seen for $2\text{-}^{57}\text{Fe}$. Complex $6\text{-}^{57}\text{Fe}$ was also produced in good yield as seen by Mössbauer spectroscopy (84%) when $1\text{-}^{57}\text{Fe}$ was treated with a previously reacted 1:1 mixture of P.A. and $\text{KO}^t\text{Bu}/18\text{-crown-6}$ at 23 °C (Scheme 4 and Figure

Scheme 4. Reaction of $[\text{Fe}^{\text{II}}(\text{CH}_3\text{CN})(\text{N}3\text{PyS})]\text{BF}_4$ and Benzenesulfinate Anion (PhSO_2^-) Sources at 23 °C


3). The latter result confirms that a 1:1 mixture of P.A. and strong base in organic solvent produces PhSO_2^- , as it does in

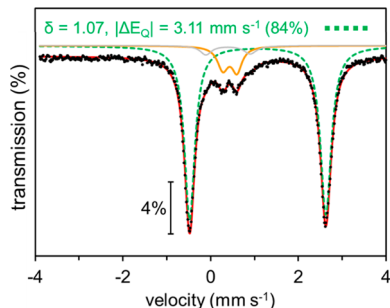


Figure 3. ^{57}Fe Mössbauer spectrum (80 K, $\text{C}_3\text{H}_7\text{CN}/\text{THF}$, 9:1 v/v) for the reaction of 1- ^{57}Fe with a previously reacted 1:1 mixture of P.A. and $\text{KO}^t\text{Bu}/18\text{-crown-6}$ at 23 °C. Experimental data (black dots); best fit (red line); $\text{Fe}^{\text{II}}(\text{PhSO}_2^-)$ adduct 6- ^{57}Fe (dashed green line, 84%); 1- ^{57}Fe (solid orange line, 12%); minor species (solid gray line, 4%) corresponding to an unidentified product.

water.⁴¹ Taken together, these experiments show that metastable **2** is not an $\text{Fe}^{\text{II}}(\text{PhSO}_2^-)$ adduct.

Next, we considered the possibility that **2** may be an Fe–HNO adduct ($\{\text{Fe}(\text{HNO})\}^8$ in the Enemark–Feltham notation). The only Mössbauer data on a proposed $\{\text{Fe}(\text{HNO})\}^8$ species comes from cryoreduction of the $\{\text{FeNO}\}^7$ adduct of taurine dioxygenase (TauD).⁵⁶ This species could only be generated in low yield (17%), but gave Mössbauer parameters of $\delta = 0.80$ and $|\Delta E_Q| = 1.64 \text{ mm s}^{-1}$ that were consistent with DFT calculations for a quintet ($S = 2$) $\{\text{Fe}(\text{HNO})\}^8$ structure. We turned to DFT methods to predict the Mössbauer parameters for $[\text{Fe}(\text{HNO})(\text{N}3\text{PyS})]^+$. Optimized geometries of the $S = 0, 1$, and 2 spin states were obtained and employed for the Mössbauer calculations (see Supporting Information). The calculated isomer shifts range from 0.27 to 0.55 mm s^{-1} (estimated maximum errors of $\pm 0.1 \text{ mm s}^{-1}$),⁵⁷ which are clearly inconsistent with the experimental data for 2- ^{57}Fe ($\delta = 1.05 \text{ mm s}^{-1}$). The calculated quadrupole splittings (estimated maximum errors of $\pm 0.5 \text{ mm s}^{-1}$)⁵⁷ are also in poor agreement with 2- ^{57}Fe . We conclude that **2** is not an Fe–HNO adduct.

Fe K-Edge X-ray Absorption Spectroscopy (XAS). The normalized X-ray absorption near-edge structure (XANES) of

complex **2** is shown in Figure 4, overlaid with the spectrum of starting **1** for comparison. The energies of the rising edge

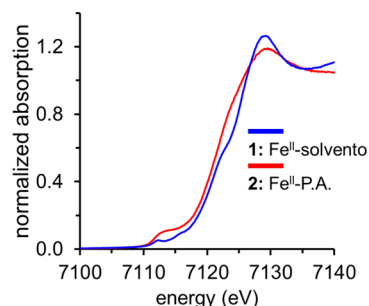


Figure 4. Normalized Fe K-edge XANES of the hs Fe^{II} –P.A. complex **2** (solid red line) and the Fe^{II} –solvento precursor **1** (solid blue line) (frozen $\text{C}_3\text{H}_7\text{CN}/\text{THF}$, 9:1 v/v).

inflection points increase upon going from **1** (7120.7 eV) to **2** (7121.5 eV), consistent with back-donation of electron density from Fe^{II} to the N–O π^* of P.A.

The extended X-ray absorption fine structure (EXAFS) of **2** is shown in Figure 5a (solid green line), along with an overlaid

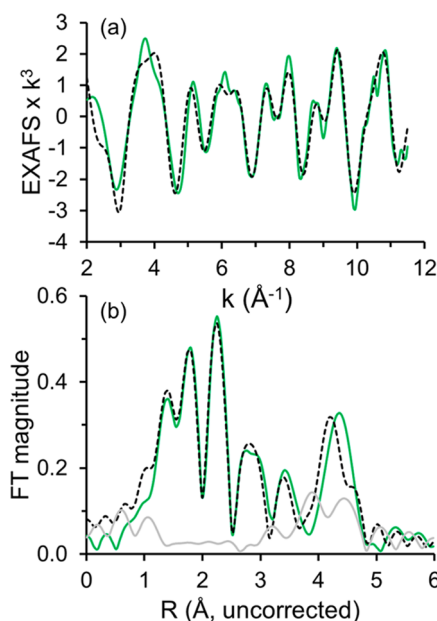


Figure 5. (a) Fe K-edge EXAFS of **2** plotted from $k = 2$ to 12 \AA^{-1} (solid green line) overlaid with the corresponding best fit (dashed black line). (b) Fourier transforms of the EXAFS data, fit, and residual (data minus fit; solid gray line).

line of best fit (dashed black line). The corresponding Fourier transforms of the EXAFS data and best fit are shown in Figure 5b. Relevant fitting parameters are provided in Table 1, and result from sequentially improved fits to the data (see Table S1). The best fit for complex **2** includes four N/O scatterers at 2.17 \AA and one S scatterer at 2.66 \AA , which correspond to the $\text{Fe}(\text{N}3\text{PyS})$ core. A fifth N/O scatterer at 1.95 \AA , an Fe–O scatterer at 2.51 \AA , and a second S scatterer at 3.25 \AA can be isolated from the data. These structural features strongly support the assignment of **2** as a hs Fe^{II} –Piloty’s acid adduct.

DFT-Calculated Structures for the Fe^{II} –Piloty’s Acid Adduct (2**).** Given the availability of EXAFS data for **2**, a constrained geometry optimization approach was employed.

Table 1. Best Fit to Fe K-edge EXAFS of Complex **2** ($F = 32.97\%$)^{a,b,c}

	CN	R (Å)	±	σ^2	±
Fe–S	1	2.66	0.01	0.005	0.001
Fe–N	4	2.17	0.01	0.010	0.001
Fe–N(O)	1	1.95	0.01	0.005	0.001
Fe–S	1	3.25	0.01	0.005	0.001
Fe–C	8	4.74	0.01	0.004	0.001
Fe–C	16	3.84	0.01	0.002	0.001
Fe–O	1	2.51	0.02	0.001	0.002

^aSee Table S1 for a list of sequentially improved fits. ^bEXAFS data were fit with EXAFSPAK using paths calculated by FEFF7. Coordination numbers were held constant, whereas distances (R) and Debye–Waller factors (σ^2) were allowed to float. Goodness of fit was measured with F , which was defined as $\left[\left(\sum_i^n [k_i^3(\text{EXAFS}_{\text{obs}} - \text{EXAFS}_{\text{calc}})]^2 / n \right)^{1/2} \right] \cdot E_0$ for the best fit was +3.64 eV. ^cTabulated errors (\pm) correspond to fitting errors. Expected errors for R are ± 0.02 Å; expected errors in CN are ca. 20–25% (ref 58).

Our computational studies commenced with quintet $[\text{Fe}^{\text{II}}(\kappa^1\text{-N-PhSO}_2\text{NOH})(\text{N3PyS})]$ (**5A**, Figure 6 and Table S3) which

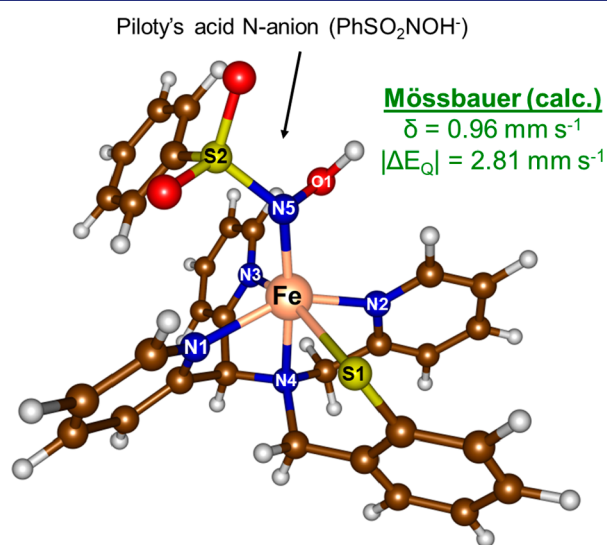


Figure 6. DFT structure of $[\text{Fe}^{\text{II}}(\kappa^1\text{-N-PhSO}_2\text{NOH})(\text{N3PyS})]$ (**5A**) obtained by optimizing with constraints from the EXAFS data for **2** (Table 1). Calculated ^{57}Fe Mössbauer parameters are shown in green. C and H atoms are depicted as brown and white spheres, respectively.

contains an N-bound, monodeprotonated P.A. ligand in the sixth coordination site. From EXAFS, the Fe–S(N3PyS), Fe–S(P.A.), Fe–N(O), and Fe...O(N) distances were fixed at 2.66, 3.25, 1.95, and 2.51 Å, respectively. The four Fe–N(N3PyS) distances, which typically have a large degree of asymmetry, were chosen such that their average would equal 2.17 Å (i.e., the EXAFS value for four Fe–N scatterers), while all remaining distances were allowed to vary. Using this spectroscopically constrained structure led to the optimized geometry shown in Figure 6. Calculation of the ^{57}Fe Mössbauer parameters for this geometry gave $\delta = 0.96$ and $|\Delta E_{\text{Q}}| = 2.81$ mm s^{-1} , both of which accord well with the experimental data for **2**- ^{57}Fe ($\delta = 1.05$ and $|\Delta E_{\text{Q}}| = 2.93$ mm s^{-1}). Similarly, when the four Fe–N(N3PyS) distances were allowed to optimize without constraints (structure **5B**, Table

S3), the calculated Mössbauer parameters were $\delta = 1.06$ and $|\Delta E_{\text{Q}}| = 2.84$ mm s^{-1} . An increase in the average Fe–N(N3PyS) distance for **5B** (2.28 Å) translates to an increase in isomer shift of ~ 0.1 mm s^{-1} , but has no impact on the calculated quadrupole splitting. Thus, EXAFS-derived structures for **2** lead to calculated Mössbauer parameters that are fully consistent with the experimental data.

Unconstrained geometry optimizations for quintet $[\text{Fe}^{\text{II}}(\kappa^1\text{-N-PhSO}_2\text{NOH})(\text{N3PyS})]$ produce shorter Fe–S(N3PyS) distances of 2.4–2.5 Å, depending on the choice of functional or basis set. These distances are not consistent with the EXAFS results. We considered the possibility that the N3PyS sulfur donor might be protonated, which could lead to elongation of the Fe–S bond. Accordingly, we investigated $[\text{Fe}^{\text{II}}(\kappa^1\text{-N-PhSO}_2\text{NO})(\text{N3PySH})]$, a tautomer of $[\text{Fe}^{\text{II}}(\kappa^1\text{-N-PhSO}_2\text{NOH})(\text{N3PyS})]$ that could be obtained by internal proton transfer from P.A. to N3PyS. Although this structure exhibits an Fe–S(N3PySH) distance of 2.60 Å, which is similar to the EXAFS-derived distance, it is ~ 20 kcal mol^{-1} higher in energy than S-deprotonated structures obtained through fully relaxed optimizations. Thus, we conclude that **5A** is the most reasonable structure for **2**. However, we cannot exclude the possibility that hydrogen bonding or other electrostatic effects (such as an $\text{N3PyS} \cdots \text{K}^+$ interaction) could contribute to elongation of the Fe–S bond in solution.

Generation of an $\{\text{FeNO}\}^7$ Complex from **2.** A rapid color change from bright red to dark brown is observed when samples of **2** are warmed to 23 °C. These changes correspond to loss of the UV–vis bands for **2** and the appearance of a species with $\lambda_{\text{max}} = 350, 450,$ and 550 nm (Figure 7). This

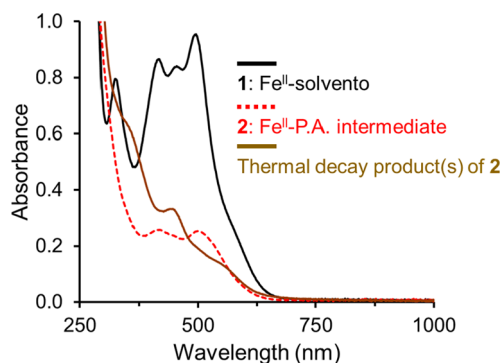


Figure 7. UV–vis spectra (CH_3CN , 0.1 mM Fe, -40 °C) comparing Fe^{II} –solvento starting material **1** (solid black line), Fe^{II} –P.A. complex **2** (dashed red line), and the thermal decay product(s) of **2** (solid brown line).

spectrum is consistent with $[\text{Fe}(\text{NO})(\text{N3PyS})]\text{BF}_4$ (**4**), an $\{\text{FeNO}\}^7$ complex previously synthesized.⁵⁹ A representative ^1H NMR spectrum of final reaction mixtures in CD_3CN is shown in Figure 8 (top), and contains a number of well-separated, paramagnetically shifted peaks between +35 and -5 ppm. These signals match the spectrum seen for **4** (Figure 8, bottom). No other paramagnetically shifted ^1H resonances are observed across the acquisition window (+130 to -50 ppm).

The generation of **4** is further evidenced by attenuated total reflectance infrared (ATR-IR) spectroscopy with ^{15}N -labeled Piloty's acid, which was synthesized according to Scheme 5. Samples of **2**- ^{57}Fe were prepared with ^{14}N –P.A. and ^{15}N –P.A. according to the standard protocol, yielding identical Mössbauer spectra which established the same purity level

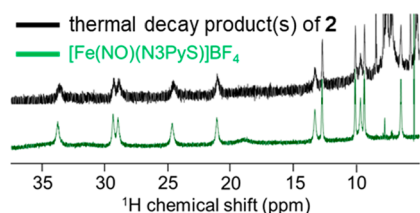
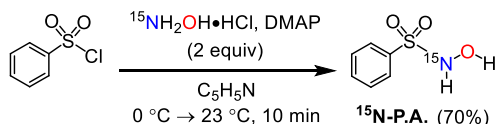


Figure 8. Paramagnetic ^1H NMR spectra (CD_3CN , $23\text{ }^\circ\text{C}$) showing the thermal decay product of **2** (top) and an authentic sample of the $\{\text{FeNO}\}^7$ complex **4** (bottom).

Scheme 5. Synthesis of ^{15}N -Labeled Piloty's Acid



for both samples (Figures S3). Warming of these samples to $23\text{ }^\circ\text{C}$ similarly yielded identical ^1H NMR spectra consistent with the $\{\text{FeNO}\}^7$ complex **4**. These samples gave the ATR-IR

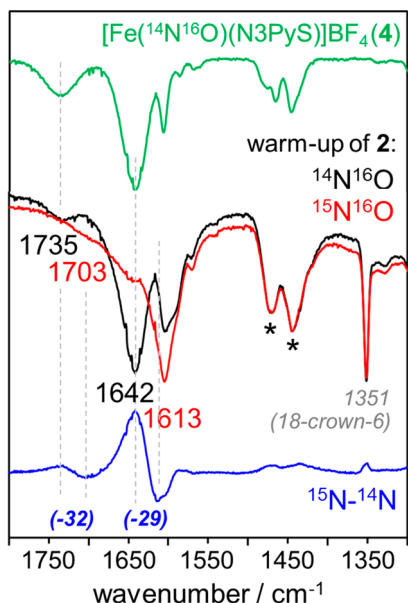


Figure 9. ATR-IR spectra following the thermal decay of **2**. Top: authentic $4\text{-}^{14}\text{N}$ (green line). Middle: thermal decay of $2\text{-}^{14}\text{N}$ (black line) and $2\text{-}^{15}\text{N}$ (red line), overlaid and normalized relative to the 1467 and 1444 cm^{-1} N3PyS ligand vibrations (denoted by *). The 1351 cm^{-1} mode originates from 18-crown-6. Bottom: difference spectrum (^{15}N minus ^{14}N , blue line) showing isotopically sensitive modes at 1735 and 1642 cm^{-1} corresponding to **4**.

spectra shown in Figure 9 (^{14}N , black line; ^{15}N , red line). The ^{15}N minus ^{14}N difference spectrum (blue line) contains a prominent band at 1642 cm^{-1} (positive intensity) that shifts to 1613 cm^{-1} (negative intensity) upon ^{15}N substitution. This band is assigned to the $\nu(\text{N}-\text{O})$ mode of **4** and exhibits a downshift of 29 cm^{-1} that is in excellent agreement with the harmonic oscillator prediction for an isolated N–O stretch (-30 cm^{-1}). A second isotopically sensitive band is observed at 1735 cm^{-1} (^{15}N : 1703 cm^{-1}), also arising from **4**. These two $\nu(\text{N}-\text{O})$ modes belong to the $S = 1/2$ and $S = 3/2$ spin states of **4**, which are both populated at $23\text{ }^\circ\text{C}$ (Figure 9, green

line).^{55,59} No other $^{14}\text{N}/^{15}\text{N}$ shifts are evident in the ATR-IR data. Importantly, these results establish that the nitrosyl ligand in **4** derives from Piloty's acid.

Mössbauer data for the thermal decay of $2\text{-}^{57}\text{Fe}$ is presented in Figure 10. Given that the spectrum of $4\text{-}^{57}\text{Fe}$ is well-resolved

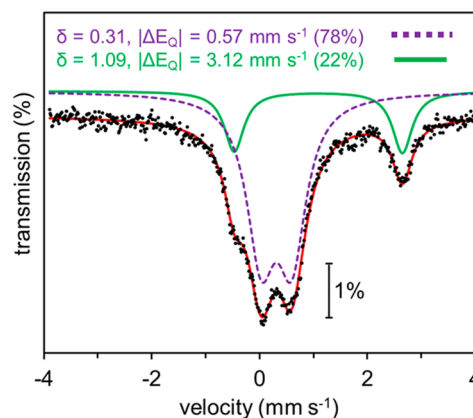


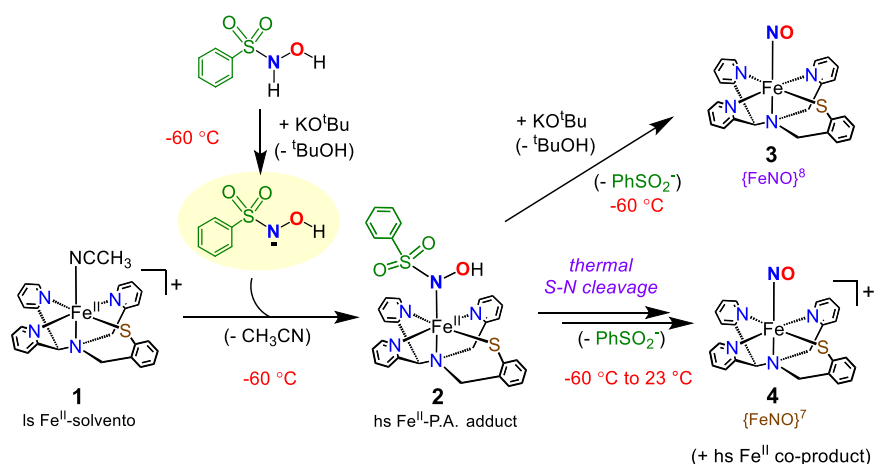
Figure 10. ^{57}Fe Mössbauer spectrum (80 K in frozen CH_3CN) showing the thermal decay of $2\text{-}^{57}\text{Fe}$. Experimental data (black dots); best fit (red line); majority $\{\text{FeNO}\}^7$ product $4\text{-}^{57}\text{Fe}$ (dashed purple line, 78%); minor hs Fe^{II} coproduct (solid green line, 22%).

at 80 K in CH_3CN (but not in mixtures of $\text{C}_3\text{H}_7\text{CN}/\text{THF}$), final reaction mixtures in $\text{C}_3\text{H}_7\text{CN}/\text{THF}$ (9:1 v/v) were concentrated to dryness under high vacuum before adding CH_3CN . The major species with $\delta = 0.31$ and $|\delta E_Q| = 0.57\text{ mm s}^{-1}$ (78% of fit) corresponds to $4\text{-}^{57}\text{Fe}$. A minor species with $\delta = 1.09$ and $|\delta E_Q| = 3.12\text{ mm s}^{-1}$ (22% of fit) is also observed, which we tentatively attribute to coordination of the PhSO_2^- byproduct at Fe. Thus, the combined data (Mössbauer, NMR, ATR-IR, and UV-vis) confirm that the major product obtained from warming **2** at -60 to $+23\text{ }^\circ\text{C}$ is the $\{\text{FeNO}\}^7$ complex **4**.

Mechanism. A mechanism for the formation and decay of Fe–P.A. complex **2** is shown in Scheme 6. Deprotonation of P.A. with $\text{KO}^t\text{Bu}/18\text{-crown-6}$ (1 equiv) at $-60\text{ }^\circ\text{C}$ affords the P.A. monoanion ($\text{PhSO}_2\text{NOH}^-$). Our data suggest that this species displaces CH_3CN from **1**, yielding P.A.-bound **2**, before HNO release can occur. The combined Mössbauer and XAS data, supported by DFT calculations, indicate that the P.A. ligand in **2** is coordinated via nitrogen. Addition of a second equivalent of $\text{KO}^t\text{Bu}/18\text{-crown-6}$ leads to the $\{\text{FeNO}\}^8$ complex **3**. In the absence of excess base, thermal decay of **2** from -60 to $+23\text{ }^\circ\text{C}$ induces S–N bond cleavage, leading to the $\{\text{FeNO}\}^7$ complex **4** (78%). There is precedent for the production of $\{\text{FeNO}\}^7$ complexes from Piloty's acid and related RSO_2NHOH compounds;^{60,61} however, these complexes were obtained from iron(III) precursors via HNO/ NO^- transfer. The production of an $\{\text{FeNO}\}^7$ complex from Piloty's acid, base, and an iron(II) precursor, as described here, is consistent with formation of a highly reactive $\{\text{Fe}(\text{HNO})\}^8$ species, which is then oxidized by an as yet unidentified pathway to give a stable $\{\text{FeNO}\}^7$ complex. Efforts are ongoing to trap the elusive nonheme $\{\text{Fe}(\text{HNO})\}^8$ species.

CONCLUSIONS

This work describes the characterization of a rare mononuclear, nonheme Fe^{II} –Piloty's acid adduct by UV-vis and ^{57}Fe Mössbauer spectroscopy, Fe K-edge XAS, and DFT. This

Scheme 6. Possible Mechanism of Formation of the Fe^{II}–Piloty’s Acid Adduct and Reaction Pathways Leading to {FeNO}⁷ and {FeNO}⁸ Products

adduct can be formed at low temperatures from an iron(II) precursor, P.A., and one equivalent of a strong alkoxide base. Piloty’s acid and related RSO₂NHOH compounds are synthetic precursors to HNO/NO⁻, and are known to react with iron(III) centers to give {FeNO}⁷ species.^{60,61} Much less is known about the reactions of RSO₂NHOH donors with iron(II) complexes, where the anticipated products are less stable, one-electron reduced {FeNO}⁸ or {Fe(HNO)}⁸ species. In this regard, we have provided strong evidence for a reaction where the P.A. donor, rather than free HNO, binds to a nonheme iron(II) complex, which then ultimately facilitates nitroxyl production on the metal. Our results indicate that binding of monoanionic P.A. to the Fe^{II} center is favored over spontaneous S–N bond cleavage to give HNO and benzenesulfinate anion (PhSO₂⁻).

Our findings also have implications for the chemistry of HNO with nonheme iron–thiolate metalloenzymes. The Fe^{II} precursor used in this study, [Fe^{II}(CH₃CN)(N3PyS)]BF₄, was previously shown to be a structural and functional mimic of the thiol dioxygenases.^{53,59} It is well-known that HNO reacts with free thiols to give sulfenamide (RS(O)NH₂) and (RSSR) products,¹² but considerably less is known about the reaction of HNO with metal-bound thiols/thiolates. In the present example, we have shown that coordination of P.A. to Fe can lead to either sulfur-ligated {FeNO}⁸ or {FeNO}⁷ species, while the sulfur donor remains unmodified. Thus, formation of a metal-bound adduct might protect sulfur sites from irreversible modification by preventing formation of free HNO from P.A. or similar HNO donors.

EXPERIMENTAL SECTION

General Procedures. All syntheses and manipulations were conducted in an N₂-filled drybox (vacuum atmospheres, O₂ < 0.2 ppm, H₂O < 0.5 ppm) or using standard Schlenk techniques under an atmosphere of dry Ar unless otherwise noted. ⁵⁷Fe powder (95.5 atom %; 98% purity) was purchased from Cambridge Isotope Laboratories. Piloty’s acid (*N*-hydroxybenzenesulfonamide) and ¹⁵N-labeled Piloty’s acid were synthesized according to a literature procedure.⁶² Potassium *tert*-butoxide (KO^tBu, sublimed grade, 99.99% trace metals basis) was purchased from Sigma-Aldrich and stored in the drybox. 18-crown-6 was purchased from Sigma-Aldrich and purified by recrystallization from hot acetonitrile. The 18-crown-6-acetonitrile solvate thus obtained was dried under high-vacuum at 35 °C for several hours to afford pure 18-crown-6. Acetonitrile, acetonitrile-*d*₃, and toluene were distilled from CaH₂. Tetrahydrofuran was distilled

from a purple sodium/benzophenone ketyl radical solution. Butyronitrile was distilled from Na₂CO₃/KMnO₄ according to a literature procedure.⁶³ Diethyl ether was obtained from a PureSolv solvent purification system (SPS) and used without further purification. All solvents were degassed by a minimum of three freeze–pump–thaw cycles and stored over freshly activated 3 Å molecular sieves in the drybox.

Instrumentation. UV–visible spectra were recorded on a Varian Cary 50 Bio spectrophotometer integrated with a Unisoku USP-203 cryostat. ¹H NMR spectra were recorded on a Bruker Avance 400 MHz FT-NMR spectrometer at 298 K and referenced against residual solvent proton signals. Attenuated total reflectance (ATR) infrared spectra were obtained with a Golden Gate Reflectance diamond cell in a Nexus 670 Thermo-Nicolet FTIR spectrometer. ⁵⁷Fe Mössbauer spectra were collected on a spectrometer from SEE Co. (Science Engineering & Education Co., MN) integrated with a Janis SVT-400-MOSS LHe/LN₂ cryostat. The spectrometer was operated in the constant acceleration mode in a transmission geometry.

[⁵⁷Fe^{II}(CH₃CN)(N3PySEtCN)](BF₄)₂ (**5-⁵⁷Fe**). The title compound was prepared as described previously²⁹ with a ⁵⁷Fe enrichment level of approximately 80%. A three-necked, 100 mL round-bottom flask equipped with a stir bar was fitted with a reflux condenser. Amounts of ⁵⁷Fe powder (33 mg, 0.58 mmol) and ⁵⁶Fe powder (11 mg, 0.20 mmol) were added. A solution of HBF₄ (48 wt % in H₂O, 0.3 mL, 2.9 equiv) was added via syringe, and the mixture was refluxed for 45 min until no Fe powder remained. The resulting aqueous solution of ⁵⁷Fe-enriched ⁵⁷Fe(BF₄)₂ was cooled to 23 °C and then diluted with CH₃CN (5 mL). The N3PySEtCN ligand (355.1 mg, 0.786 mmol) was dissolved in CH₃CN (10 mL), and the ⁵⁷Fe(BF₄)₂ solution was added at 23 °C, producing an immediate color change from pale orange to dark red-orange. After 2 h, excess Et₂O (20 mL) was added, resulting in precipitation of a brown residue. The supernatant was decanted by cannula, and the residue was dried *in vacuo* over P₄O₁₀. Slow vapor diffusion of Et₂O into a concentrated CH₃CN solution of the product furnished large red crystals of **5-⁵⁷Fe** after 24 h (413 mg, 73% yield).

[⁵⁷Fe^{II}(CH₃CN)(N3PyS)]BF₄ (**1-⁵⁷Fe**). The title compound was prepared as described previously²⁹ with a ⁵⁷Fe enrichment level of approximately 80%. An amount of crystalline **5-⁵⁷Fe** (81 mg, 0.11 mmol) was dissolved with vigorous stirring in CH₃CN (4 mL). A slurry of KO^tBu (13 mg, 0.11 mmol, 1 equiv) in CH₃CN (2 mL) was prepared and added dropwise at 23 °C to the solution of **5-⁵⁷Fe**, resulting in an immediate color change from dark red-orange to dark wine red. The mixture was stirred for 2.5 h, filtered through a short plug of Celite, and concentrated under reduced pressure. The dark red-brown residue was triturated with Et₂O (3 × 5 mL) and dried to yield crude **1-⁵⁷Fe**. The crude product was dissolved in a mixture of CH₃CN and toluene (1:1 v/v, 4 mL) and filtered through Celite.

Excess Et₂O (12 mL) was added, and the turbid mixture was placed in a -35 °C freezer overnight, resulting in precipitation of a red-brown microcrystalline solid. Removal of the yellow-brown supernatant and further drying under reduced pressure yielded pure 1-⁵⁷Fe (42 mg, 65% yield).

⁵⁷Fe Mössbauer Spectroscopy. ⁵⁷Fe Mössbauer spectra were collected on frozen solution samples at 80 K in the absence of an applied magnetic field. ⁵⁷Fe-enriched samples were prepared in custom Delrin cups (10.0 mm × 12.4 mm OD) equipped with tight-fitting Delrin inserts (5.0 mm × 11.0 mm). All samples were stored under LN₂ prior to analysis. The zero velocity of each Mössbauer spectrum refers to the centroid of a 25 μm metallic iron (α-Fe) foil collected at room temperature. The WMOSS program (SEE Co., formerly WEB Research Co., Edina, MN) was used to analyze the Mössbauer data. Data were fit to quadrupole doublets with Lorentzian or Voigt line shapes as specified.

Fe K-Edge X-ray Absorption Spectroscopy. Fe K-edge XAS and extended X-ray absorption fine structure (EXAFS) data were collected at the 16-pole, 2-T wiggler Beamline 9-3 at the Stanford Synchrotron Radiation Lightsource (SSRL) under ring conditions of 500 mA and 3 GeV. All samples were ⁵⁷Fe-enriched in order to assess purity by Mössbauer spectroscopy, and were prepared in custom screw-top Delrin Mössbauer cups. The base of each cup contained a slit (1 × 4 mm) that was covered in 38 μM Kapton tape to provide an X-ray transparent window, thus allowing for sequential Mössbauer and XAS measurements. Samples were maintained at 10 K in an Oxford liquid He flow cryostat. A Si(220) double-crystal monochromator was used for energy selection. A Rh-coated mirror (set to an energy cutoff of 9 keV) was used for harmonic rejection. Internal incident energy calibration was achieved by assigning the first inflection points of a Fe foil placed downstream of the sample to 7111.2 eV. Data were collected in fluorescence mode using a Canberra 30-element Ge array detector windowed on Fe Kα emission. Elastic scatter into the detector was attenuated using a Soller slit with an upstream Co filter. Multiple scans were measured and averaged with SIXPACK⁶⁴ software package. No spectral changes due to photodamage were observed after multiple scans for these complexes. Data were normalized to postedge jumps of 1.0 at 7130 eV in SIXPACK by applying a Gaussian normalization for the pre-edge and a three-region cubic spline to model the smooth background above the edge. EXAFS data were fitted using the OPT module of EXAFSPAK⁶⁵ using initial scattering paths calculated using FEFF7.^{66,67}

Generation of 2-⁵⁷Fe. A dark red solution of 1-⁵⁷Fe (5 mg, 9 μmol) in C₃H₇CN (1.6 mL) was combined with a stir bar in a 10 mL Schlenk flask. The flask was cooled to -60 °C in a slurry of dry ice and chloroform. A stock solution of Piloty's acid (9 mg, 53 μmol) in C₃H₇CN (1.15 mL) was prepared, and an aliquot (200 μL, 9 μmol, 1 equiv per Fe) was loaded into a gastight syringe. A stock solution of KO^tBu (6 mg, 50 μmol) and 18-crown-6 (13 mg, 50 μmol) in THF (1.1 mL) was prepared, and an aliquot (200 μL, 9 μmol, 1 equiv per Fe) was loaded into a separate gastight syringe. The Piloty's acid solution was added dropwise over 10 min to the solution of 1-⁵⁷Fe at -60 °C, and stirring was continued for an additional 5 min. Next, the KO^tBu/18-crown-6 solution was added dropwise over 10 min. Stirring was continued for 2 h, over which time the color of the reaction mixture turned from dark wine red to bright pink red. For Mössbauer spectroscopy, the reaction mixture was poured into liquid N₂, and the resulting frozen powder was packed into a sample cup under liquid N₂. Alternatively, the reaction mixture was further cooled to -98 °C, and transferred by precooled syringe to a precooled sample cup. Samples for Fe K-edge X-ray absorption spectroscopy were prepared in an identical manner.

Reaction of 1-⁵⁷Fe with Previously Reacted 1:1 Mixture of Piloty's Acid and KO^tBu/18-crown-6 at 23 °C. Piloty's acid (15 mg, 87 μmol) was dissolved in C₃H₇CN (1.0 mL). Amounts of KO^tBu (11 mg, 94 μmol) and 18-crown-6 (24 mg, 90 μmol) were combined and dissolved in THF (1.0 mL). The solution of KO^tBu/18-crown-6 was added to the solution of Piloty's acid with stirring, resulting in a dark yellow mixture. The color of the reaction mixture

rapidly bleached within ~5 s. Stirring was continued for 48 h at 23 °C, at which point the mixture appeared colorless and slightly turbid.

An amount of 1-⁵⁷Fe (2 mg, 3 μmol) was dissolved in C₃H₇CN (600 μL). An aliquot of the previously reacted P.A./KO^tBu/18-crown-6 mixture (80 μL; 3 μmol, 1 equiv per Fe based on initial P.A.) was added dropwise to 1-⁵⁷Fe, resulting in an immediate color change from dark wine-red to bright pink-red. For Mössbauer spectroscopy, an aliquot of the reaction mixture (400 μL) was transferred to a sample cup and frozen in liquid N₂.

Reaction of 1-⁵⁷Fe with NaPhSO₂ at 23 °C. An amount of 1-⁵⁷Fe (2 mg, 3 μmol) was dissolved in a mixture of C₃H₇CN (500 μL) and THF (50 μL). Sodium benzenesulfinate (11 mg, 66 μmol) and 18-crown-6 (18 mg, 70 μmol) were combined with C₃H₇CN (1.0 mL), and the resulting slurry was vigorously stirred for 1 h. An amount of the slurry (60 μL; 4 μmol Na⁺PhSO₂⁻) was added dropwise to 1-⁵⁷Fe with continued stirring, producing an immediate color change from dark wine-red to bright pink-red. For Mössbauer spectroscopy, an aliquot of the reaction mixture (400 μL) was transferred to a sample cup and frozen in liquid N₂.

■ ASSOCIATED CONTENT

📄 Supporting Information

The Supporting Information is available free of charge on the ACS Publications website at DOI: 10.1021/jacs.9b01700.

⁵⁷Fe Mössbauer data/fits, Fe K-edge EXAFS data/fits, and DFT calculations (PDF)

■ AUTHOR INFORMATION

Corresponding Authors

*E-mail: dpg@jhu.edu

*E-mail: kml236@cornell.edu

ORCID

Alex M. Confer: 0000-0002-9922-894X

Aniruddha Dey: 0000-0001-7162-0483

Kyle M. Lancaster: 0000-0001-7296-128X

David P. Goldberg: 0000-0003-4645-1045

Notes

The authors declare no competing financial interest.

■ ACKNOWLEDGMENTS

The NSF (CHE1566007 to D.P.G.) and NIH (R35GM124908 to K.M.L.) are gratefully acknowledged for financial support. A.M.C. thanks the Harry and Cleio Greer Fellowship for support. XAS data were obtained at the Stanford Synchrotron Radiation Lightsource (SSRL). Use of SSRL, SLAC National Accelerator Laboratory, is supported by the U.S. Department of Energy, Office of Science, Office of Basic Energy Sciences under Contract No. DE-AC02-76SF00515. The SSRL Structural Molecular Biology Program is supported by the DOE Office of Biological and Environmental Research, and by the National Institutes of Health, National Institute of General Medical Sciences (including P41GM103393). The Kirin cluster at JHU KSAS is thanked for CPU time to A.M.C.

■ REFERENCES

- (1) Suarez, S. A.; Muñoz, M.; Alvarez, L.; Venâncio, M. F.; Rocha, W. R.; Bikiel, D. E.; Martí, M. A.; Doctorovich, F. HNO Is Produced by the Reaction of NO with Thiols. *J. Am. Chem. Soc.* **2017**, *139*, 14483–14487.
- (2) Kumar, M. R.; Clover, T.; Olaitan, A. D.; Becker, C.; Solouki, T.; Farmer, P. J. The reaction between GSNO and H₂S: On the generation of NO, HNO and N₂O. *Nitric Oxide* **2018**, *77*, 96–105.

- (3) Suarez, S. A.; Neuman, N. I.; Muñoz, M.; Álvarez, L.; Bikiel, D. E.; Brondino, C. D.; Ivanović-Burmazović, I.; Miljković, J.; Filipović, M. R.; Martí, M. A.; Doctorovich, F. Nitric oxide is reduced to HNO by proton-coupled nucleophilic attack by ascorbate, tyrosine, and other alcohols. A new route to HNO in biological media? *J. Am. Chem. Soc.* **2015**, *137*, 4720–4727.
- (4) Hamer, M.; Suarez, S. A.; Neuman, N. I.; Alvarez, L.; Munoz, M.; Marti, M. A.; Doctorovich, F. Discussing endogenous NO-/HNO interconversion aided by phenolic drugs and vitamins. *Inorg. Chem.* **2015**, *54*, 9342–9350.
- (5) Irvine, J. C.; Ritchie, R. H.; Favaloro, J. L.; Andrews, K. L.; Widdop, R. E.; Kemp-Harper, B. K. Nitroxyl (HNO): the Cinderella of the nitric oxide story. *Trends Pharmacol. Sci.* **2008**, *29*, 601–608.
- (6) Paolucci, N.; Jackson, M. I.; Lopez, B. E.; Miranda, K.; Tocchetti, C. G.; Wink, D. A.; Hobbs, A. J.; Fukuto, J. M. The pharmacology of nitroxyl (HNO) and its therapeutic potential: not just the Janus face of NO. *Pharmacol. Ther.* **2007**, *113*, 442–458.
- (7) Tocchetti, C. G.; Wang, W.; Froehlich, J. P.; Huke, S.; Aon, M. A.; Wilson, G. M.; Di Benedetto, G.; O'Rourke, B.; Gao, W. D.; Wink, D. A.; Toscano, J. P.; Zaccolo, M.; Bers, D. M.; Valdivia, H. H.; Cheng, H.; Kass, D. A.; Paolucci, N. Nitroxyl improves cellular heart function by directly enhancing cardiac sarcoplasmic reticulum Ca²⁺ cycling. *Circ. Res.* **2007**, *100*, 96–104.
- (8) Nagasawa, H. T.; DeMaster, E. G.; Redfern, B.; Shirota, F. N.; Goon, D. J. W. Evidence for nitroxyl in the catalase-mediated bioactivation of the alcohol deterrent agent cyanamide. *J. Med. Chem.* **1990**, *33*, 3120–3122.
- (9) DeMaster, E. G.; Redfern, B.; Nagasawa, H. T. Mechanisms of inhibition of aldehyde dehydrogenase by nitroxyl, the active metabolite of the alcohol deterrent agent cyanamide. *Biochem. Pharmacol.* **1998**, *55*, 2007–2015.
- (10) Shoeman, D. W.; Shirota, F. N.; DeMaster, E. G.; Nagasawa, H. T. Reaction of nitroxyl, an aldehyde dehydrogenase inhibitor, with N-acetyl-L-cysteine. *Alcohol* **2000**, *20*, 55–59.
- (11) Miller, T. W.; Cherney, M. M.; Lee, A. J.; Francoleon, N. E.; Farmer, P. J.; King, S. B.; Hobbs, A. J.; Miranda, K. M.; Burstyn, J. N.; Fukuto, J. M. The effects of nitroxyl (HNO) on soluble guanylate cyclase activity: interactions at ferrous heme and cysteine thiols. *J. Biol. Chem.* **2009**, *284*, 21788–21796.
- (12) Bianco, C. L.; Toscano, J. P.; Bartberger, M. D.; Fukuto, J. M. The chemical biology of HNO signaling. *Arch. Biochem. Biophys.* **2017**, *617*, 129–136.
- (13) Einsle, O.; Messerschmidt, A.; Huber, R.; Kroneck, P. M. H.; Neese, F. Mechanism of the six-electron reduction of nitrite to ammonia by cytochrome c nitrite reductase. *J. Am. Chem. Soc.* **2002**, *124*, 11737–11745.
- (14) Guo, Y.; Stroka, J. R.; Kandemir, B.; Dickerson, C. E.; Bren, K. L. A Cobalt Metallopeptide Electrocatalyst for the Selective Reduction of Nitrite to Ammonium. *J. Am. Chem. Soc.* **2018**, *140*, 16888–16892.
- (15) Anderson, J. H. The metabolism of hydroxylamine to nitrite by Nitrosomonas. *Biochem. J.* **1964**, *91*, 8–17.
- (16) Lin, R.; Farmer, P. J. The HNO adduct of myoglobin: Synthesis and characterization. *J. Am. Chem. Soc.* **2000**, *122*, 2393–2394.
- (17) Sulc, F.; Fleischer, E.; Farmer, P. J.; Ma, D.; La Mar, G. N. ¹H NMR structure of the heme pocket of HNO-myoglobin. *J. Biol. Inorg. Chem.* **2003**, *8*, 348–352.
- (18) Sulc, F.; Immoos, C. E.; Pervitsky, D.; Farmer, P. J. Efficient trapping of HNO by deoxymyoglobin. *J. Am. Chem. Soc.* **2004**, *126*, 1096–1101.
- (19) Immoos, C. E.; Sulc, F.; Farmer, P. J.; Czarnecki, K.; Bocian, D. F.; Levina, A.; Aitken, J. B.; Armstrong, R. S.; Lay, P. A. Bonding in HNO-myoglobin as characterized by X-ray absorption and resonance Raman spectroscopies. *J. Am. Chem. Soc.* **2005**, *127*, 814–815.
- (20) Pervitsky, D.; Immoos, C.; van der Veer, W.; Farmer, P. J. Photolysis of the HNO adduct of myoglobin: transient generation of the aminoxyl radical. *J. Am. Chem. Soc.* **2007**, *129*, 9590–9591.
- (21) Kumar, M. R.; Pervitsky, D.; Chen, L.; Poulos, T.; Kundu, S.; Hargrove, M. S.; Rivera, E. J.; Diaz, A.; Colón, J. L.; Farmer, P. J. Nitrosyl hydride (HNO) as an O₂ analogue: long-lived HNO adducts of ferrous globins. *Biochemistry* **2009**, *48*, 5018–5025.
- (22) Montenegro, A. C.; Amorebieta, V. T.; Slep, L. D.; Martin, D. F.; Roncaroli, F.; Murgida, D. H.; Bari, S. E.; Olabe, J. A. Three redox states of nitrosyl: NO⁺, NO[•], and NO⁻/HNO interconvert reversibly on the same pentacyanoferrate(II) platform. *Angew. Chem., Int. Ed.* **2009**, *48*, 4213–4216.
- (23) Montenegro, A. C.; Bari, S. E.; Olabe, J. A. Reactivity of iron(II)-bound nitrosyl hydride (HNO, nitroxyl) in aqueous solution. *J. Inorg. Biochem.* **2013**, *118*, 108–114.
- (24) Walter, M. R.; Dzul, S. P.; Rodrigues, A. V.; Stemmler, T. L.; Telser, J.; Conradie, J.; Ghosh, A.; Harrop, T. C. Synthesis of Co^{II}-NO⁻ Complexes and Their Reactivity as a Source of Nitroxyl. *J. Am. Chem. Soc.* **2016**, *138*, 12459–12471.
- (25) Goodrich, L. E.; Roy, S.; Alp, E. E.; Zhao, J.; Hu, M. Y.; Lehnert, N. Electronic structure and biologically relevant reactivity of low-spin {FeNO}⁸ porphyrin model complexes: new insight from a bis-picket fence porphyrin. *Inorg. Chem.* **2013**, *52*, 7766–7780.
- (26) Abucayon, E. G.; Khade, R. L.; Powell, D. R.; Zhang, Y.; Richter-Addo, G. B. Hydride Attack on a Coordinated Ferric Nitrosyl: Experimental and DFT Evidence for the Formation of a Heme Model-HNO Derivative. *J. Am. Chem. Soc.* **2016**, *138*, 104–107.
- (27) Kumar, M. R.; Zapata, A.; Ramirez, A. J.; Bowen, S. K.; Francisco, W. A.; Farmer, P. J. Nitrosyl hydride (HNO) replaces dioxygen in nitroxigenase activity of manganese quercetin dioxygenase. *Proc. Natl. Acad. Sci. U. S. A.* **2011**, *108*, 18926–18931.
- (28) Han, X.; Kumar, M. R.; Farmer, P. J. Nitroxigenation of quercetin by HNO. *Tetrahedron Lett.* **2016**, *57*, 399–402.
- (29) Confer, A. M.; McQuilken, A. C.; Matsumura, H.; Moënnelocoz, P.; Goldberg, D. P. A Nonheme, High-Spin {FeNO}⁸ Complex that Spontaneously Generates N₂O. *J. Am. Chem. Soc.* **2017**, *139*, 10621–10624.
- (30) Patra, A. K.; Dube, K. S.; Sanders, B. C.; Papaefthymiou, G. C.; Conradie, J.; Ghosh, A.; Harrop, T. C. A thermally stable {FeNO}⁸ complex: properties and biological reactivity of reduced MNO systems. *Chem. Sci.* **2012**, *3*, 364–369.
- (31) Sanders, B. C.; Patra, A. K.; Harrop, T. C. Synthesis, properties, and reactivity of a series of non-heme {FeNO}^{7/8} complexes: implications for Fe-nitroxyl coordination. *J. Inorg. Biochem.* **2013**, *118*, 115–127.
- (32) Rhine, M. A.; Rodrigues, A. V.; Bieber Urbauer, R. J.; Urbauer, J. L.; Stemmler, T. L.; Harrop, T. C. Proton-induced reactivity of NO⁻ from a {CoNO}⁸ complex. *J. Am. Chem. Soc.* **2014**, *136*, 12560–12563.
- (33) Rhine, M. A.; Sanders, B. C.; Patra, A. K.; Harrop, T. C. Overview and new insights into the thiol reactivity of coordinated NO in {MNO}^{6/7/8} (M = Fe, Co) complexes. *Inorg. Chem.* **2015**, *54*, 9351–9366.
- (34) Speelman, A. L.; White, C. J.; Zhang, B.; Alp, E. E.; Zhao, J.; Hu, M.; Krebs, C.; Penner-Hahn, J.; Lehnert, N. Non-heme High-Spin {FeNO}^{6–8} Complexes: One Ligand Platform Can Do It All. *J. Am. Chem. Soc.* **2018**, *140*, 11341–11359.
- (35) Kupper, C.; Schober, A.; Demeshko, S.; Bergner, M.; Meyer, F. An exclusively organometallic {FeNO}⁷ complex with tetracarbene ligation and a linear FeNO unit. *Inorg. Chem.* **2015**, *54*, 3096–3098.
- (36) Pellegrino, J.; Bari, S. E.; Bikiel, D. E.; Doctorovich, F. Successful stabilization of the elusive species {FeNO}⁸ in a heme model. *J. Am. Chem. Soc.* **2010**, *132*, 989–995.
- (37) Garcia-Serres, R.; Grapperhaus, C. A.; Bothe, E.; Bill, E.; Weyhermüller, T.; Neese, F.; Wieghardt, K. Structural, spectroscopic, and computational study of an octahedral, non-heme {FeNO}^{6–8} Series: [Fe(NO)(cyclam-ac)]^{2+/+/0}. *J. Am. Chem. Soc.* **2004**, *126*, 5138–5153.
- (38) Li, F.; Meyer, R. L.; Carpenter, S. H.; VanGelder, L. E.; Nichols, A. W.; Machan, C. W.; Neidig, M. L.; Matson, E. M. Nitric oxide activation facilitated by cooperative multimetallic electron transfer within an iron-functionalized polyoxovanadate-alkoxide cluster. *Chem. Sci.* **2018**, *9*, 6379–6389.

- (39) Shafirovich, V.; Lymar, S. V. Nitroxyl and its anion in aqueous solutions: spin states, protic equilibria, and reactivities toward oxygen and nitric oxide. *Proc. Natl. Acad. Sci. U. S. A.* **2002**, *99*, 7340–7345.
- (40) Buchholz, J. R.; Powell, R. E. The Decomposition of Hyponitrous Acid. I. The Non-chain Reaction. *J. Am. Chem. Soc.* **1963**, *85*, 509–511.
- (41) DuMond, J. F.; King, S. B. The chemistry of nitroxyl-releasing compounds. *Antioxid. Redox Signaling* **2011**, *14*, 1637–1648.
- (42) Zhou, Y.; Cink, R. B.; Fejedelem, Z. A.; Cather Simpson, M.; Seed, A. J.; Sampson, P.; Brasch, N. E. Development of Photo-activatable Nitroxyl (HNO) Donors Incorporating the (3-Hydroxy-2-naphthalenyl)methyl Phototrigger. *Eur. J. Org. Chem.* **2018**, *2018*, 1745–1755.
- (43) Carrone, G.; Pellegrino, J.; Doctorovich, F. Rapid generation of HNO induced by visible light. *Chem. Commun.* **2017**, *53*, 5314–5317.
- (44) Piloty, O. Ueber eine Oxydation des Hydroxylamins durch Benzolsulfchlorid. *Ber. Dtsch. Chem. Ges.* **1896**, *29*, 1559–1567.
- (45) Di Fiore, A.; Maresca, A.; Alterio, V.; Supuran, C. T.; De Simone, G. Carbonic anhydrase inhibitors: X-ray crystallographic studies for the binding of N-substituted benzenesulfonamides to human isoform II. *Chem. Commun.* **2011**, *47*, 11636–11638.
- (46) Exner, O. Acyl derivatives of hydroxylamine. IX. A spectroscopic study of tautomerism of sulphohydroxamic acids. *Collect. Czech. Chem. Commun.* **1964**, *29*, 1337–1343.
- (47) Exner, O.; Juška, T. X-ray photoelectron spectroscopic study of sulphonamides: Charge distribution and tautomerism. *Collect. Czech. Chem. Commun.* **1984**, *49*, 51–57.
- (48) Álvarez, L.; Suarez, S. A.; Bikiel, D. E.; Reboucas, J. S.; Batinić-Haberle, I.; Martí, M. A.; Doctorovich, F. Redox potential determines the reaction mechanism of HNO donors with Mn and Fe porphyrins: defining the better traps. *Inorg. Chem.* **2014**, *53*, 7351–7360.
- (49) Bonner, F. T.; Ko, Y. Kinetic, Isotopic, and ^{15}N NMR Study of N-hydroxybenzenesulfonamide Decomposition: An HNO Source Reaction. *Inorg. Chem.* **1992**, *31*, 2514–2519.
- (50) Martí, M. A.; Bari, S. E.; Estrin, D. A.; Doctorovich, F. Discrimination of nitroxyl and nitric oxide by water-soluble Mn(III) porphyrins. *J. Am. Chem. Soc.* **2005**, *127*, 4680–4684.
- (51) Subedi, H.; Brasch, N. E. Mechanistic studies of the reactions of the reduced vitamin B₁₂ derivatives with the HNO donor Piloty's acid: further evidence for oxidation of cob(I)alamin by (H)NO. *Dalton Trans.* **2016**, *45*, 352–360.
- (52) Dey, A.; Confer, A. M.; Vilbert, A. C.; Moëne-Loccoz, P.; Lancaster, K. M.; Goldberg, D. P. A Nonheme Sulfur-Ligated {FeNO}⁶ Complex and Comparison with Redox-Interconvertible {FeNO}⁷ and {FeNO}⁸ Analogues. *Angew. Chem., Int. Ed.* **2018**, *57*, 13465–13469.
- (53) McQuilken, A. C.; Jiang, Y.; Siegler, M. A.; Goldberg, D. P. Addition of dioxygen to an N₄S(thiolate) iron(II) cysteine dioxygenase model gives a structurally characterized sulfinate-iron(II) complex. *J. Am. Chem. Soc.* **2012**, *134*, 8758–8761.
- (54) Widger, L. R.; Jiang, Y.; McQuilken, A. C.; Yang, T.; Siegler, M. A.; Matsumura, H.; Moëne-Loccoz, P.; Kumar, D.; de Visser, S. P.; Goldberg, D. P. Thioether-ligated iron(II) and iron(III)-hydroperoxo/alkylperoxo complexes with an H-bond donor in the second coordination sphere. *Dalton Trans.* **2014**, *43*, 7522–7532.
- (55) McQuilken, A. C.; Matsumura, H.; Dürr, M.; Confer, A. M.; Sheckelton, J. P.; Siegler, M. A.; McQueen, T. M.; Ivanović-Burmazović, I.; Moëne-Loccoz, P.; Goldberg, D. P. Photoinitiated Reactivity of a Thiolate-Ligated, Spin-Crossover Nonheme {FeNO}⁷ Complex with Dioxygen. *J. Am. Chem. Soc.* **2016**, *138*, 3107–3117.
- (56) Ye, S.; Price, J. C.; Barr, E. W.; Green, M. T.; Bollinger, J. M., Jr.; Krebs, C.; Neese, F. Cryoreduction of the NO-adduct of taurine:alpha-ketoglutarate dioxygenase (TauD) yields an elusive {FeNO}⁸ species. *J. Am. Chem. Soc.* **2010**, *132*, 4739–4751.
- (57) Pápai, M.; Vankó, G. On Predicting Mössbauer Parameters of Iron-Containing Molecules with Density-Functional Theory. *J. Chem. Theory Comput.* **2013**, *9*, 5004–5020.
- (58) Riggs-Gelasco, P. J.; Stemmler, T. L.; Penner-Hahn, J. E. XAFS of dinuclear metal sites in proteins and model compounds. *Coord. Chem. Rev.* **1995**, *144*, 245–286.
- (59) McQuilken, A. C.; Ha, Y.; Sutherlin, K. D.; Siegler, M. A.; Hodgson, K. O.; Hedman, B.; Solomon, E. I.; Jameson, G. N. L.; Goldberg, D. P. Preparation of non-heme {FeNO}⁷ models of cysteine dioxygenase: sulfur versus nitrogen ligation and photorelease of nitric oxide. *J. Am. Chem. Soc.* **2013**, *135*, 14024–14027.
- (60) Davies, S. C.; Evans, D. J.; Hughes, D. L.; Konkol, M.; Richards, R. L.; Sanders, J. R.; Sobota, P. Mononuclear, binuclear, trinuclear and tetranuclear iron complexes of the N(CH₂CH₂S)₃³⁻ (NS₃) ligand with nitrosyl co-ligands. *J. Chem. Soc., Dalton Trans.* **2002**, 2473–2482.
- (61) Suárez, S. A.; Martí, M. A.; De Biase, P. M.; Estrin, D. A.; Bari, S. E.; Doctorovich, F. HNO trapping and assisted decomposition of nitroxyl donors by ferric hemes. *Polyhedron* **2007**, *26*, 4673–4679.
- (62) Aizawa, K.; Nakagawa, H.; Matsuo, K.; Kawai, K.; Ieda, N.; Suzuki, T.; Miyata, N. Piloty's acid derivative with improved nitroxyl-releasing characteristics. *Bioorg. Med. Chem. Lett.* **2013**, *23*, 2340–2343.
- (63) Armarego, W. L. F.; Perrin, D. D. *Purification of Laboratory Chemicals*, 4th ed.; Butterworth-Heinemann: Oxford, 1997.
- (64) Webb, S. *SIXPACK, Stanford Synchrotron Lightsource*; Stanford Linear Accelerator Center, Stanford University: Stanford, CA, 2002.
- (65) George, G. N. *EXAFSPAK*; Stanford Synchrotron Radiation Lightsource, S. L. A. C. Stanford University.
- (66) Mustre de Leon, J.; Rehr, J. J.; Zabinsky, S. I.; Albers, R. C. Ab initio curved-wave x-ray-absorption fine structure. *Phys. Rev. B: Condens. Matter Mater. Phys.* **1991**, *44*, 4146–4156.
- (67) Rehr, J. J.; Mustre de Leon, J.; Zabinsky, S. I.; Albers, R. C. Theoretical x-ray absorption fine structure standards. *J. Am. Chem. Soc.* **1991**, *113*, 5135–5140.